Electronic and optical properties of polyicosahedral Si nanostructures: A first-principles study

Kengo Nishio,[1,*] Taisuke Ozaki,[1,2] Tetsuya Morishita,[1] Wataru Shinoda,[1] and Masuhiro Mikami[1]

[1]*Research Institute for Computational Sciences (RICS), National Institute of Advanced Industrial Science and Technology (AIST), Central 2, Umezono 1-1-1, Tsukuba, Ibaraki 305-8568, Japan*

[2]*Research Center for Integrated Science (RCIS), Japan Advanced Institute of Science and Technology (JAIST), 1-1 Asahidai, Nomi, Ishikawa 923-1292 Japan*

(Received 27 June 2007; revised manuscript received 13 December 2007; published 27 February 2008)

In a previous molecular dynamics study, we predicted a polyicosahedral Si nanostructure which has a Si_{20} fullerene cage per icosahedral Si_{100} nanodot. The unique cage structure is distinct from the crystalline diamond Si nanostructure. Encapsulating a guest atom into the Si_{20} cage allows us to tune the electronic and optical properties. Here, we report on a systematic first-principles study of the effect of the sodium and iodine doping on the physical properties of the hydrogen-terminated polyicosahedral Si nanostructures. Our calculations reveal the strongly guest-dependent and size-dependent physical properties of the polyicosahedral Si nanostructures: (1) the semiconducting guest-free polyicosahedral nanowire becomes metallic by the sodium and iodine doping, (2) the quantum confinement effect is observed in the icosahedral and polyicosahedral nanodots, and (3) the radiative recombination rate comparable to the luminescent amorphous Si nanostructures is expected from some of the Na- and I-doped polyicosahedral nanostructures. From these results, we assert that the polyicosahedral Si nanostructures are promising candidates for the building blocks of the future nanoscale optoelectronic devices.

DOI: 10.1103/PhysRevB.77.075431 PACS number(s): 73.22.−f, 73.21.La, 73.21.Hb, 73.61.Wp

I. INTRODUCTION

Low-dimensional Si nanostructures (NSs), such as Si nanodots (Si NDs) and Si nanowires (Si NWs), have attracted much attention because of the potential uses in the future nanoscale devices. The physical properties of Si NSs dramatically depend on the size and arrangement of Si atoms. For example, Si NSs of different sizes emit different colors of light, and the radiative recombination rate of amorphous Si NSs is higher than that of crystalline diamond Si (cd-Si) NSs.[1,2] The stable atomic arrangement also depends on the size of Si NSs, and, interestingly enough, the atomic arrangements not seen in bulk Si could be found in Si NSs due to the large surface-to-volume ratio.[3–10] Therefore, enormous efforts have been devoted to explore novel Si NSs.

The stability of Si fullerenes has been studied since the discovery of carbon fullerenes. Although both Si and carbon are members of the group IV of the Periodic Table, single-shell Si fullerenes, such as Si_{20} and Si_{60}, are found to be unstable.[3,11] This is because the nature of bonding is very different between Si and carbon. Carbon atoms can be joined together by sp^2 bonding to form fullerene structures without dangling bonds. On the other hand, Si atoms prefer sp^3 bonding so that Si fullerenes inevitably have dangling bonds which make Si fullerenes unstable. There are several efforts to stabilize Si fullerenes by encapsulating atoms into Si fullerenes.[12–21]

The existence of icosahedral Si (i-Si) NDs $(Si_{100}, Si_{280}, Si_{600}, \ldots)$ has been suggested by a series of studies.[6,8] Recent first-principles calculations have shown that pristine icosahedral Si (i-Si) NDs are energetically more stable than pristine cd-Si NDs for diameters of less than 2.77 nm.[6] Our molecular dynamics (MD) simulations using the Tersoff potential[22] have demonstrated that an icosahedral Si_{280} ND is spontaneously formed by freezing a droplet.[8] The i-Si NDs can be regarded as multishell Si fullerenes. For example, the icosahedral Si_{280} ND is a $Si_{20}@Si_{80}@Si_{180}$ triple-shell Si fullerene, in which the Si_{80} fullerene is stabilized by encapsulating a Si_{20} fullerene and the Si_{180} fullerene is stabilized by encapsulating a $Si_{20}@Si_{80}$ double-shell fullerene. Unlike carbon fullerenes, Si atoms in the Si fullerenes are arranged in rugged shells because all the atoms are joined by sp^3 bonding. Each Si atom is bonded to three atoms within the same shell and to an atom within an adjacent shell. Thus, all the Si atoms except for some atoms in the outermost shell are four coordinated.

Several possible structure models have also been proposed for the Si NW.[5,7,23–27] Recently, we have predicted the existence of polyicosahedral Si (pi-Si) NWs $(Si_{150}, Si_{420}, Si_{900}, \ldots)$.[7] Our MD simulations have demonstrated that the polyicosahedral Si_{150} NW composed of linked icosahedral Si_{100} ND is spontaneously formed by freezing liquid Si inside a nanopore, and that the pi-Si NW is stable even in a vacuum up to about 77% of the melting temperature of bulk cd-Si. Furthermore, our structural energy calculations have revealed that the pi-Si NW is the lowest-energy form of one-dimensional Si known so far, at least for diameters of less than 6.02 nm.

The frameworks of Si having fullerene cages, such as Si_{20}, Si_{24}, and Si_{28} cages, are known as Si clathrates. Three types of Si clathrate, types I, II and III, have been synthesized in the bulk (three-dimensional) system.[28,29] Various kinds of guest atoms can be encapsulated into the fullerene cages of the bulk Si clathrates. For example, Na-, Ba-, and I-doped Si clathrates have been synthesized.[28–31] The nature of the electronic band structure depends on the guest atoms. The first-principles calculations have shown that the guest-free type-I Si clathrate (Si_{46}) is a semiconductor.[32] On the other hand, $Na_xBa_{8-x}@Si_{46}$ and $I_8@Si_{46}$ are metals.[33–35] The stabilities of Si clathrate NWs cut out bulk Si clathrates, the

Si_{20} cage polymer and Si_{24} cage polymer, and the effects of atom encapsulation on the electronic structures of these Si clathrate NWs have been studied.[36–39] The pi-Si NS (N_l-PINS), which is constructed by linking N_l icosahedra together, has a Si_{20} cage per i-Si ND, and therefore it can be regarded as a novel low-dimensional Si clathrate. Note that the 1-PINS is a i-Si ND, the 2-PINS is a pi-Si ND constructed by linking two icosahedra together, and the ∞-PINS is a pi-Si NW. These pi-Si NSs cannot be made by cutting out bulk Si clathrates.

The unique cage structure of the pi-Si NS is distinct from the cd-Si NS. Encapsulating a guest atom into the Si_{20} cage allows us to tune the electronic and optical properties. In the present paper, we carry out a systematic first-principles study of the effect of sodium and iodine doping on the electronic and optical properties of the pi-Si NS. The surface dangling bonds of Si NSs are usually terminated by hydrogen, oxygen, or nitrogen atoms in experiment. In our study, we focus on the hydrogen-terminated (H-terminated) pi-Si NSs: the icosahedral $Si_{100}H_{60}$ ND (1-PINS), the polyicosahedral $Si_{175}H_{90}$ ND (2-PINS), and the polyicosahedral $Si_{150}H_{60}$ NW (∞-PINS). We also compare the electronic structure of the guest-free pi-Si NW with those of the pentagonal Si (pent-Si), NW ($Si_{30}H_{10}$ NW), and cd-Si NW ($Si_{45}H_{20}$ NW).[5,7]

II. MODEL AND METHOD

A. Electronic structure calculation

The electronic structure of Si NSs is calculated by the density functional theory[40,41] (DFT) within the local density approximation (LDA).[42,43] Norm-conserving pseudopotentials are used in a separable form with multiple projectors to replace the deep core potential into a shallow potential.[44,45] The wave functions are expressed by the linear combination of atomic orbitals centered on atomic sites. The atomic basis functions are generated by solving atomic Kohn-Sham equations using confinement pseudopotentials.[46,47] The primitive pseudoatomic basis sets Si6.5-*s*2*p*2*d*1, Na8.0-*s*2*p*1, and I8.0-*s*1*p*1*d*1 are used for Si, Na, and I atoms, respectively, where the abbreviation, for example, Si6.5-*s*2*p*2*d*1, represents the employment of two primitive *s* orbitals, two primitive *p* orbitals, and one primitive *d* orbital of a Si atom which are generated with a confinement radius of 6.5 bohr. The contracted pseudoatomic basis set, H5.5-*s*52, is used for H atoms, where *s*52 represents that two *s* orbitals are generated by contracting five primitive *s* orbitals of a H atom. The contraction coefficients are optimized to minimize the total energy of the $Si_{20}H_{20}$ cluster. The contracted bases improve the accuracy of the calculation without increasing the computational cost. The real space grid techniques are used with the cutoff energy of about 200 Ry, when calculating Hamiltonian matrix elements and solving the Poisson equation with a fast Fourier transformation.[48] The Γ point, five *k*-point, and three *k*-point samplings are used for the Brillouin zone sampling in the case of the polyicosahedral $Si_{150}H_{60}$ NW, pentagonal $Si_{30}H_{10}$ NW, and crystalline diamond $Si_{45}H_{20}$ NW, respectively. The size of the simulation box is set so that the wave functions do not overlap with their images.

TABLE I. The optimized length L of a unit cell in the direction of the wire axis and the diameter $d=\sqrt{a^3N/2\pi L}$, where a is the lattice constant of bulk cd-Si (0.5365 nm in our theoretical framework) and N is the number of Si atoms in the unit cell.

	L (nm)	d (nm)
$Si_{150}H_{60}$ NW	1.706	1.47
$Na_2@Si_{150}H_{60}$ NW	1.710	1.47
$I_2@Si_{150}H_{60}$ NW	1.705	1.47
$NaI@Si_{150}H_{60}$ NW	1.711	1.47
$Si_{30}H_{10}$ NW	0.3819	1.39
$Si_{45}H_{20}$ NW	0.52669	1.45

All the calculations are carried out using the OpenMX code.[49] In order to check our methods, we have calculated the electronic band structures of bulk type-I Si clathrates, Si_{46}, $Na_8@Si_{46}$, and $I_8@Si_{46}$, and confirmed that our calculations reproduce the literature well.[33–35]

B. Geometry optimization

The pristine icosahedral Si_{100} ND ($Si_{20}@Si_{80}$ double-shell fullerene) consists of 20 slightly distorted crystalline tetrahedra Si_5.[6] The tetrahedron has four (111) nanofacets, and the adjacent tetrahedra are joined by forming covalent bonds between Si atoms in facing (111) facets. All the Si atoms in the Si_{100} ND are joined by tetrahedral bonding. The pristine polyicosahedral Si_{175} ND is constructed by linking two Si_{100} NDs together by sharing five crystalline tetrahedra. Thus, the Si_{175} ND contains two Si_{20} cages. The pristine polyicosahedral Si_{150} NW is constructed by linking Si_{100} NDs periodically together and has a Si_{20} cage per Si_{100} ND.[7]

First, we place the pristine pi-Si NSs in simulation boxes so that the fivefold symmetry axis coincides with the *z* axis and optimize the geometries by a steepest decent method using the empirical Tersoff model.[22] Second, we terminate surface dangling bonds of the pristine Si NSs by hydrogen atoms. The H-terminated Si NSs, the icosahedral $Si_{100}H_{60}$ ND, the polyicosahedral $Si_{175}H_{90}$ ND, and the polyicosahedral $Si_{150}H_{60}$ NW, are relaxed by a direct inversion in the iterative subspace method[50] using the OpenMX until the force on each atom becomes 0.0001 hartree/bohr or less. Third, we place a Na or an I atom on the gravity center of each Si_{20} cage. The doped Si NSs are then relaxed again. The optimized length of a unit cell of a pi-Si NW in the *z* direction (the wire direction) is determined by comparing total energies calculated for different lengths. We summarize the optimized lengths of unit cells in Table I.

For comparison, we optimize the structure of the H-terminated pentagonal $Si_{30}H_{20}$ NW.[5,7] The pent-Si NW is composed of five crystalline triangular prisms which are cut out cd-Si. The prism is oriented toward the (110) direction and has two (111) and one H-terminated (100) facets with dimerization. The adjacent prisms are joined by forming covalent bonds between Si atoms in facing (111) facets, and each prism exposes the (100) facet. We also optimize the

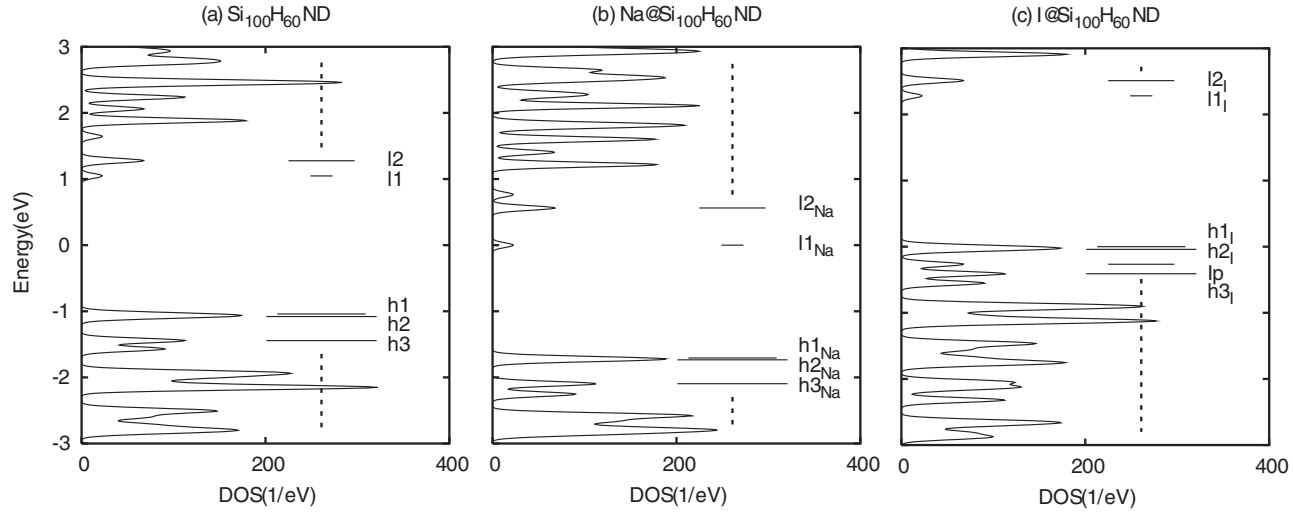

FIG. 1. The electronic structures of (a) $Si_{100}H_{60}$ ND, (b) Na@$Si_{100}H_{60}$ ND, and (c) I@$Si_{100}H_{60}$ ND. Energy is measured from the Fermi energy E_F, −4.38, −3.75, and −5.43 eV for (a), (b), and (c), respectively. The density of states is shown on the left-hand side. The discrete spectrum is smeared out by a Gaussian broadening method with a width of 0.05 eV. The energy and degeneracy of states near the E_F are illustrated by the horizontal lines on the right-hand side.

structure of the H-terminated crystalline diamond $Si_{45}H_{20}$ NW,[7] which is oriented toward the (100) direction and exposes four H-terminated (110) facets and four H-terminated (100) facets with dimerization.

III. GUEST-FREE POLYICOSAHEDRAL SILICON NANOSTRUCTURES

A. Electronic and optical properties

The electronic structures of the 1-PINS (icosahedral $Si_{100}H_{60}$ ND), 2-PINS (polyicosahedral $Si_{175}H_{90}$ ND), and ∞-PINS (polyicosahedral $Si_{150}H_{60}$ NW) are shown in Figs. 1(a), 2(a), and 3(a), respectively. Note that the electronic bands shown in Fig. 3(a) are folded at X point because the screw symmetry is not considered in the unit cell.[51] We refer to the upper (lower) parts of the C1, V1, and V2 bands to the $C1^{+(-)}$, $V1^{+(-)}$, and $V2^{+(-)}$ bands, respectively.

The l1, l2, h1, h2, and h3 states of the i-Si ND belong to the A_g, T_{1u}, G_g, H_u, and H_g representations of the point group I_h, respectively. By comparing electron wave functions of the 1-PINS to those of the 2-PINS and ∞-PINS (Appendix A), we find that the wave function $\Psi^{\mu}_{N_l}$ of the N_l-PINS is well expressed as linear combinations of wave functions $\phi^{\nu}_{N_l}$ which resemble the wave function Ψ^{ν}_1 of the 1-PINS, where the μ and ν are the indices of electronic state. This information will help us understand the effects of encapsulating Na and I atoms into the Si_{20} cages.

The band gap energy $E_g(N_l)$ increases from 1.20, 1.60, to 2.09 eV as the number of linked i-Si NDs N_l decreases from ∞, 2, to 1.[52] The size-dependent band gap energy of the polyicosahedral Si NSs is explained by the quantum confinement effect. As the system size increases, the DFT calculation soon becomes practically impossible due to high computational costs. For calculating the band gap energies of

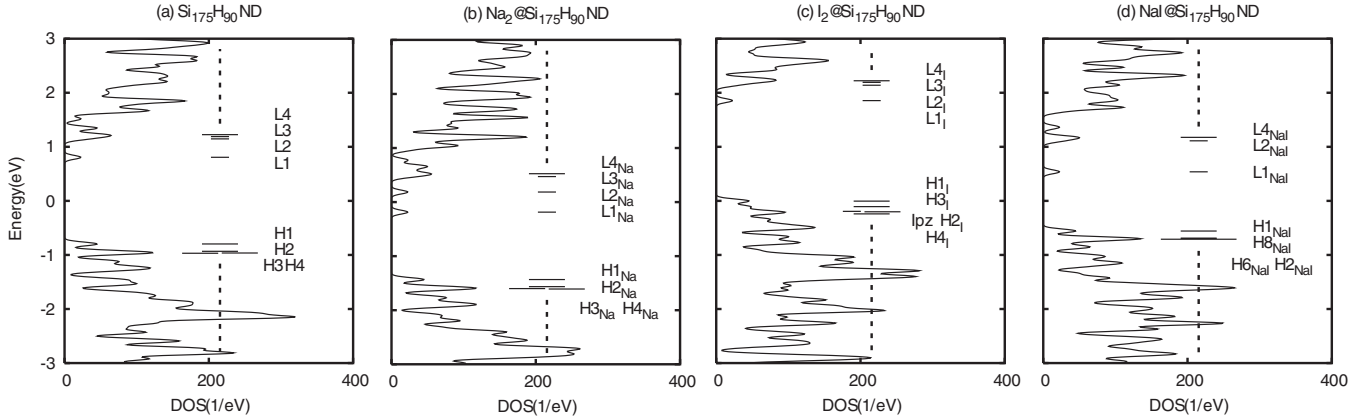

FIG. 2. The electronic structures of (a) $Si_{175}H_{90}$ ND, (b) Na_2@$Si_{175}H_{90}$ ND, (c) I_2@$Si_{175}H_{90}$ ND, and (d) NaI@$Si_{175}H_{90}$ ND. Energy is measured from the Fermi energy E_F, −4.36, −3.75, −5.16, and −4.55 eV for (a), (b), (c), and (d), respectively. The density of states is shown on the left-hand side. The discrete spectrum is smeared out by a Gaussian broadening method with a width of 0.05 eV. The energy and degeneracy of states near the E_F are illustrated by the horizontal lines on the right-hand side.

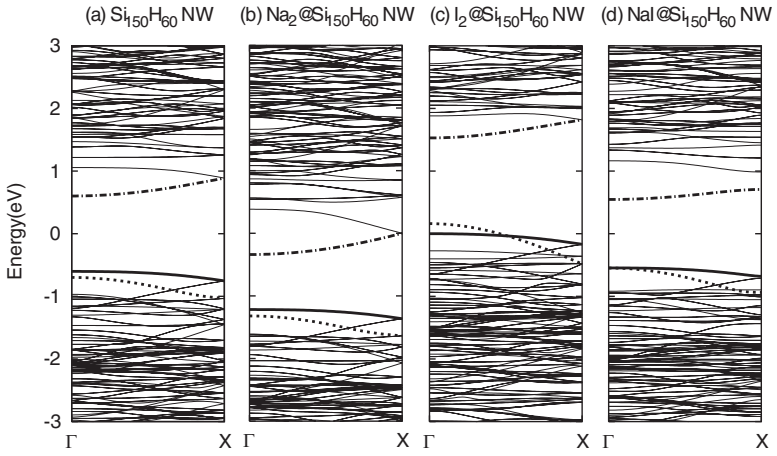

FIG. 3. The electronic band structures of (a) $Si_{150}H_{60}$ NW, (b) $Na_2@Si_{150}H_{60}$ NW, (c) $I_2@Si_{150}H_{60}$ NW, and (d) $NaI@Si_{150}H_{60}$ NW. Energy is measured from the Fermi energy E_F, −4.38, −3.83, −4.98, and −4.47 eV for (a), (b), (c), and (d), respectively. The $C1^-_G$, $V1^+_G$, and $V2^+_G$ bands are drawn in bold dot-dashed, solid, and dotted lines, respectively.

longer N_l-PINSs ($N_l > 2$), the method based on an effective mass approximation (EMA) is useful. It is known that although the EMA is not a good approximation for the smallest nanostructures, it properly describes the electronic structures of larger nanostructures.[53] Thus, the DFT and EMA methods could be complementary to each other to calculate the band gap energy in the wide size range. Using the EMA with the infinite well potential, the band gap energy of the N_l-PINS is given as

$$E_g^{\mathrm{EMA}}(N_l) = E_g(\infty) + \frac{\pi^2\hbar^2}{2(LN_l/2)^2}\left(\frac{1}{m_c^*} + \frac{1}{m_v^*}\right), \qquad (1)$$

where $E_g(\infty)$ is the band gap energy of the polyicosahedral $Si_{150}H_{60}$ NW, 1.20 eV, $\hbar$ is the Planck constant divided by 2π, and L is the optimized length of the unit cell of the pi-Si NW in the direction of the wire axis. There are two i-Si NDs in a unit cell so that $LN_l/2$ represents the length of the N_l-PINS. The effective masses of conduction and valence bands [at $C1^-(\Gamma)$ and $V1^+(\Gamma)$ states] of the pi-Si NW are determined from Fig. 3(a) as $m_c^* = 0.40m_e$ and $m_v^* = 1.71m_e$, respectively, where m_e is the mass of electron. Figure 4 shows the size dependence of band gap energy. Although the EMA overestimates the band gap energy of the 1-PINS, it reproduces that of the 2-PINS well. Therefore, the band gap energies of longer N_l-PINSs ($N_l > 2$) should be properly estimated by Eq. (1).

One might expect that the pi-Si NW emits light efficiently because it has a direct band gap. Within the electronic dipole approximation, the radiative recombination rate $P_{\mu c,\mu' v}$ between the level μ in the conduction band (c) and level μ' in the valence band (v) is expressed as[54]

$$P_{\mu c,\mu' v} = \frac{1}{\tau_{\mu c,\mu' v}} = \frac{4n_0\alpha[E_{\mu c} - E_{\mu' v}]}{3m_e^2\hbar c^2}|\langle\Psi_{\mu c}|\hat{p}|\Psi_{\mu' v}\rangle|^2, \qquad (2)$$

where $\tau_{\mu c,\mu' v}$ is the radiative recombination time, n_0 is the refraction index (for which we set $n_0 = 1$), α is the fine-structure constant, and c is the velocity of light. The momentum operator is denoted by $\hat{p}$, and $\Psi_{\mu c}$ and $\Psi_{\mu' v}$ represents the electronic wave functions of the μc and $\mu' v$ states, respectively, while $E_{\mu c}$ and $E_{\mu' v}$ are the corresponding energy levels. The lowest unoccupied molecular orbital (LUMO) [$C1^-(\Gamma)$] and highest occupied molecular orbital (HOMO) [$V1^+(\Gamma)$] of the pi-Si NW belong to the A_{1g} and E_{1g} representations in the point group D_{5v}, respectively, while $\hat{p}_\perp$ ($\hat{p}_x$ and $\hat{p}_y$) and $\hat{p}_z$ belong to the E_{1u} and A_{2u} representations, respectively. Since the product $A_{1g} \times E_{1g}$ does not contain the E_{1u} and A_{2u} representations, the momentum matrix element $\langle\Psi_{\mathrm{LUMO}}|\hat{p}|\Psi_{\mathrm{HOMO}}\rangle$ is zero, and the optical dipole transition is prohibited. Therefore, the pi-Si NW does not emit light efficiently, even though it is a direct-band-gap semiconductor. We have also confirmed that the optical dipole transition between the LUMO and HOMO states is prohibited in the i-Si ND and the pi-Si ND due to the selection rule. Thus, N_l-PINSs are not suitable for light emitting devices as they are. However, as we shall show later, the radiative recombination rates of the i-Si ND, pi-Si ND, and pi-Si NW can be enhanced by encapsulating Na or I atoms into their Si_{20} cages.

B. Comparison with other Si nanowires

The pristine pi-Si NW is the most stable one-dimensional Si known so far, while the pristine pent-Si NW is the second most stable.[7] The pi-Si NW exposes the (111) facets only which has the lowest surface energy, and the highest stability is explained by the surface energy minimization. The relative

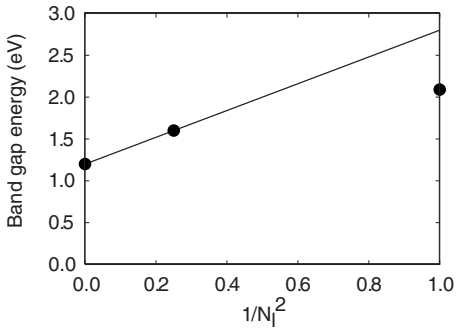

FIG. 4. The size dependence of the band gap energy of the N_l-PINS. The circles are obtained from the DFT calculations. The solid line is obtained from Eq. (1).

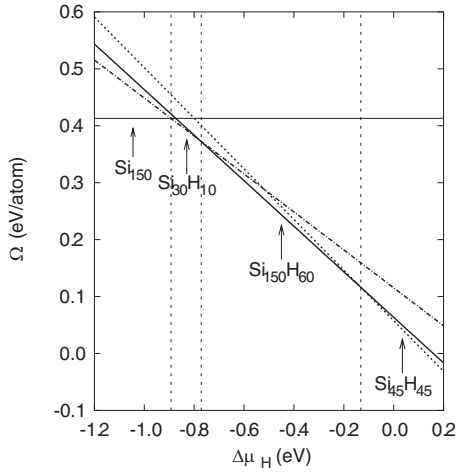

FIG. 5. The formation energy Ω of H-terminated Si NWs as a function of hydrogen chemical potential $\Delta\mu_H$. The solid, dot-dashed, and dashed lines are results for the polyicosahedral $Si_{150}H_{60}$ NW, pentagonal $Si_{30}H_{10}$ NW, and crystalline diamond $Si_{45}H_{20}$ NW, respectively. The thin horizontal line is the result for the pristine polyicosahedral Si_{150} NW calculated using the Tersoff potential (Ref. 7). The vertical dashed lines indicate transition energies.

stabilities might change by passivating surface dangling bonds by hydrogen atoms.[6,55] The formation energy Ω of a H-terminated Si NW at zero temperature as a function of the hydrogen chemical potential μ_H is defined as[56]

$$\Omega(\mu_H) = E + n_H e_0 - n_{Si}\mu_{Si} - n_H\mu_H, \quad (3)$$

where E is the total energy of the Si NW, e_0 is the zero-point energy arising from a Si-H vibrational mode, μ_{Si} is the chemical potential of bulk cd-Si, and n_{Si} and n_H are the numbers of Si and H atoms, respectively. If we measure the μ_H relative to the μ_H^* at which the formation energy of a SiH_4 molecule is equal to zero, Eq. (3) becomes

$$\Omega(\Delta\mu_H) = E - n_H\left(\Delta\mu_H + \frac{E_{SiH_4} - \mu_{Si}}{4}\right) - n_{Si}\mu_{Si}, \quad (4)$$

where $\Delta\mu_H = \mu_H - \mu_H^*$, and E_{SiH_4} is the total energy of a SiH_4 molecule. The larger value of $\Delta\mu_H$ means that the Si NW is placed in the hydrogen richer environment. As a reference, we note that the most stable phase of the H-terminated Si (001) bulk surface changes from the 2×1 monohydride structure to the 3×1 monohydride plus dihydride structure when $\Delta\mu_H$ exceeds −0.24 eV, and then the most stable phase changes to the 1×1 dihydride structure when $\Delta\mu_H$ exceeds −0.09 eV.[56] The formation energies per Si atom of the polyicosahedral $Si_{150}H_{60}$ NW, the pentagonal $Si_{30}H_{10}$ NW, and the crystalline diamond $Si_{45}H_{20}$ NW are shown in Fig. 5. We also show the energy of the pristine polyicosahedral Si_{150} NW calculated using the Tersoff potential[7] in Fig. 5. Note that the diameters of the pi-Si, pent-Si, and cd-Si NWs are similar to each other, 1.47, 1.39, and 1.45 nm, respectively (Table I). Figure 5 reveals that the most stable structure changes according to the hydrogen chemical potential. The pristine pi-Si NW is the most stable for $\Delta\mu_H < -0.89$ eV. The transition from the pristine pi-Si NW to the H-terminated pent-Si NW occurs when μ_H exceeds −0.89 eV, and the H-terminated pent-Si NW is the most stable until $\Delta\mu_H$ exceeds −0.77 eV. The transition from the H-terminated pent-Si NW to the H-terminated pi-Si NW occurs at $\mu_H = -0.77$ eV, and the H-terminated pi-Si NW is the most stable in the range $-0.77 < \Delta\mu_H < -0.13$ eV. For $-0.13\ \text{eV} < \Delta\mu_H$, the cd-Si NW is the most stable. This trend is explained by means of the ratio of H atoms to Si atoms. The H/Si ratios of the polyicosahedral Si_{150} NW, the pentagonal $Si_{30}H_{10}$ NW, the polyicosahedral $Si_{150}H_{60}$ NW, and crystalline diamond $Si_{45}H_{20}$ NW are 0.00, 0.33, 0.40, and 0.44, respectively. The structure with a higher H/Si ratio becomes more stable as $\Delta\mu_H$ increases, and the most stable structure changes. Although the pi-Si NW and pent-Si NW have not been identified experimentally yet, our results suggest that the hydrogen chemical potential could be a key for synthesizing these Si NWs.

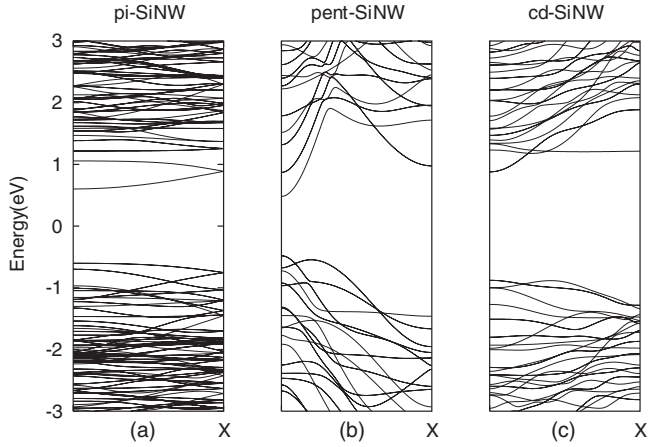

FIG. 6. The electronic band structures of (a) polyicosahedral $Si_{150}H_{60}$ NW, (b) pentagonal $Si_{30}H_{10}$ NW, and (c) crystalline diamond $Si_{45}H_{20}$ NW. Energy is measured from the Fermi energy E_F.

The electronic band structures of the pi-Si, pent-Si, and cd-Si NWs depicted in Fig. 6 reveal that all the Si NWs are direct-band-gap semiconductors, while the bulk cd-Si is an indirect-band-gap semiconductor. However, the optical dipole transition between the LUMO and HOMO states is prohibited in the pent-Si and cd-Si NWs due to the selection rule as well as the pi-Si NW. The band gap energy strongly depends on the wire structure as is summarized in Table II. The cd-Si NW has the largest band gap energy, 1.76 eV. The second is the pi-Si NW, 1.20 eV. The smallest is the pent-Si NW, 0.96 eV. All the band gap energies are larger than the

TABLE II. The band gap energy and the conduction and valence band effective masses for the polyicosahedral $Si_{150}H_{60}$ NW, the pentagonal $Si_{30}H_{10}$ NW, and the crystalline diamond $Si_{45}H_{20}$ NW. m_e is the mass of electron.

	E_g (eV)	m_c^*/m_e	m_v^*/m_e
pi-Si NW	1.20	0.40	1.71
pent-Si NW	0.96	0.13	0.19
cd-Si NW	1.76	0.27	0.91

bulk cd-Si (0.51 eV in our theoretical framework). The effective masses of the Si NWs at the valence band maximum and conduction band minimum are also summarized in Table II. The effective masses of the pent-Si NW are considerably small compared to those of the pi-Si NW and cd-Si NW, indicating that carriers in the pent-Si NW might have large mobilities for the diffusive transport.

IV. DOPED POLYICOSAHEDRAL SILICON NANOSTRUCTURES

A. Electronic structure of Na-doped systems

By calculating the encapsulation energy, we find that encapsulating Na atoms into the Si_{20} cages of the pi-Si NSs is possible (Appendix C). The electronic structure of the $Na@Si_{100}H_{60}$ ND is shown in Fig. 1(b). By comparing the wave functions (not shown), we have confirmed that the electronic states labeled by li_{Na} and hi_{Na} originate in the l*i* and h*i* states of the $Si_{100}H_{60}$ ND, respectively. Due to the greater electropositivity of sodium, one valence electron is transferred from the Na atom to the host $Si_{100}H_{60}$ ND so that the $l1_{Na}$ state of the $Na@Si_{100}H_{60}$ ND is half filled. The effects of the orbital coupling between the i-Si ND and the Na atom are explained as follows. In our calculations, the 2*p*, 3*s*, and 4*s* orbitals of a Na atom are used as basis functions. The *s* and *p* states belong to the A_g and T_{1u} representations in the point group I_h, respectively. Therefore, the states of the $Si_{100}H_{60}$ ND, which belongs to the A_g (l1 state) and T_{1u} (l2 state) representations, couple with the sodium *s* and *p* states, respectively, while the other states (h1, h2, and h3 states) do not. Actually, the sodium *s* states hybridize with the l1 state of the i-Si ND, and the $l1_{Na}$ state shifts downward in energy due to the bonding hybridization. Although the l2 states of the i-Si ND couples with the sodium *p* state, the hybridization effect is negligibly small. As a result, the level spacing between the $l2_{Na}$ (LUMO) and $l1_{Na}$ (HOMO) states (0.56 eV) is enlarged compared with the spacing between the l2 and l1 states (0.23 eV). Interestingly, the optical dipole transition between the $l2_{Na}$ and $l1_{Na}$ states of the $Na@Si_{100}H_{60}$ ND is possible with a radiative recombination rate of 1.0×10^6 s^{-1}, which is comparable to the rates of luminescent amorphous Si NDs.[2]

The electronic structure of the $Na_2@Si_{175}H_{90}$ ND is shown in Fig. 2(b). The electronic states labeled by Li_{Na} and Hi_{Na} originate in the L*i* and H*i* states of the $Si_{175}H_{90}$ ND, respectively. The $L1_{Na}$ state is filled with two valence electrons from the two Na atoms. The band gap energy, the level spacing between the $L2_{Na}$ and $L1_{Na}$ states, is 0.37 eV. The LUMO-HOMO optical dipole transition is possible ($P_{L2_{Na},L1_{Na}}=1.0\times10^6$ s^{-1}). Since the wave functions of the L2 and L1 states of the pi-Si ND have the $\phi_2^{A_g}$ component (Appendix A), these states hybridize with the sodium *s* states. Due to the bonding hybridization, the $L2_{Na}$ and $L1_{Na}$ states shift downward in energy. As in the case of the $Na@Si_{100}H_{60}$ ND, the hybridization effect of the sodium *p* state near the Fermi level is negligibly small.

The electronic structure of the $Na_2@Si_{150}H_{60}$ NW is shown in Fig. 3(b). The $C1_{Na}$, $V1_{Na}$, and $V2_{Na}$ bands of the $Na_2@Si_{150}H_{60}$ NW originate in the C1, V1, and V2 bands of the $Si_{150}H_{60}$ NW, respectively. The guest-free pi-Si NW is a semiconductor, while the Na-doped pi-Si NW is a metal because the $C1_{Na}$ band is half filled with valence electrons from Na atoms. From Table V, it is considered that the wave functions $\phi_\infty^{A_g}$ and $\phi_\infty^{T_{1u}[A_1]}$ are mixed in the C1 band of the pi-Si NW, and the ratio of the $\phi_\infty^{A_g}$ component decreases as the state changes from $C1^-(\Gamma)$, $C1(X)$, to $C1^+(\Gamma)$. Thus, the C1 band, particularly near the $C1^-(\Gamma)$ state, hybridizes strongly with sodium *s* states. As a result, the bandwidth of the $C1_{Na}$ band is enlarged. As in the case of the $Na@Si_{100}H_{60}$ ND, the hybridization effect of the sodium *p* state near the Fermi level is negligibly small.

One-dimensional structures with partially filled metallic bands often undergo the Peierls distortion when they are relaxed using a larger unit cell,[57] accompanying a metal-semiconductor transition in which the bands split into the lower-energy filled bands and the higher-energy empty bands. The Peierls instability is determined by the competition between the decrease in electronic energy and the increase in distortion energy. The thinner structure is more unstable against the Peierls distortion.[58,59] The Na-doped pi-Si NW might undergo the Peierls transition, since the $C1_{Na}$ band of the $Na_2@Si_{150}H_{60}$ NW is half filled. In order to check the Peierls instability, we optimized the geometry of the Na-doped pi-Si NW using a double-size unit cell, the $Na_4@Si_{300}H_{120}$ NW, which is prepared by replicating the $Na_2@Si_{150}H_{60}$ NW. Note that the geometry optimization is carried out using a length of the unit cell in the *z* direction, 2×17.10 Å. By analyzing the band structure of the optimized $Na_4@Si_{300}H_{120}$ NW (not shown), we have confirmed that the $Na_4@Si_{300}H_{120}$ NW is a metal and the effect of Peierls distortion is negligibly small.

Figure 7 compares the electronic band structures of partially Na-doped pi-Si NWs, $Na_x@Si_{300}H_{120}$ NWs. The geometry of the $Na_x@Si_{300}H_{120}$ NW is prepared by replicating the optimized $Na_2@Si_{150}H_{60}$ NW and removing $(4-x)$ Na atoms. The electronic structures are calculated without geometry optimization because we have confirmed that there is no significant difference in the electronic structure near the Fermi level between the optimized $Na_2@Si_{150}H_{60}$ NW and the initial structure, the optimized $Si_{150}H_{60}$ NW with a Na atom placed at the gravity center of each Si_{20} cage. There are four Si_{20} cages per unit cell so that there are five possible doping patterns: |OXXX|, |OXOX|, |OOXX|, |OOOX|, and |OOOO|, where O and X indicate doped and empty Si_{20} cages, respectively. The band structure of the |OOOO| NW is obtained by folding the bands of the $Na_2@Si_{150}H_{60}$ NW. Therefore, the number of bands become double. Accordingly, we refer the lower and upper parts of the $C1_{Na}^-$ band to the $C1_{Na}^{--}$ and $C1_{Na}^{-+}$ bands, respectively. Due to the symmetry reduction which depends on doping pattern, there appear energy gaps in the C1 bands of partially Na-doped pi-Si NWs. The |OXXX|, |OXOX|, and |OOOX| NWs are metals as in the case of the |OOOO| NW. Interestingly, the |OOXX| NW is a direct-band-gap semiconductor with a 0.24 eV energy gap. The optical dipole transition between the $C1_{Na}^{-+}(X)$ and $C1_{Na}^{--}(X)$ states is possible with a recombination rate of 3.2×10^6 s^{-1}.

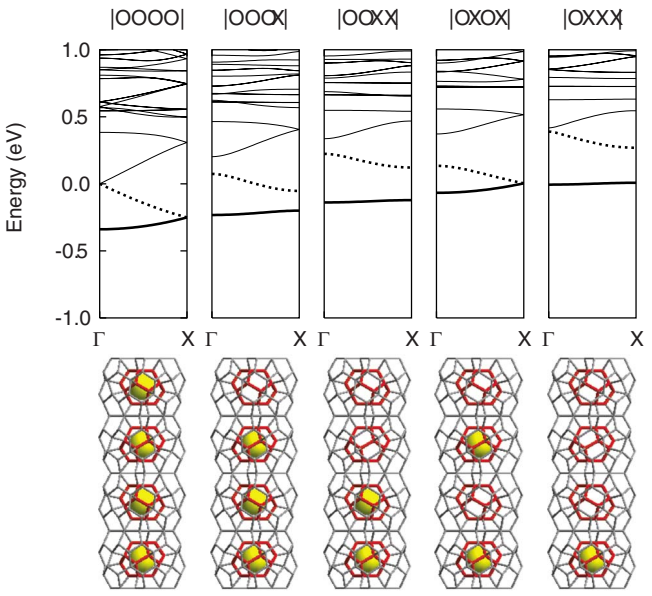

FIG. 7. (Color online) The electronic band structures of partially Na-doped pi-Si NWs, $Na_x@Si_{300}H_{120}$ NWs. Energy is measured from the Fermi energy E_F, −3.83, −3.88, −3.93, −3.95, and −3.97 eV for |OOOO|, |OOOX|, |OOXX|, |OXOX|, and |OXXX| NWs, respectively. The $C1^{--}_{Na}$ and $C1^{++}_{Na}$ bands are drawn in bold solid and dotted lines, respectively. The unit cell is given below each band. The Si–Si bonds are depicted. The bold (red) bonds represent Si_{20} cages. Spheres are guest atoms. Note that Si–H bonds are not shown for clarity.

B. Electronic structure of I-doped systems

By calculating the encapsulation energy, we find that encapsulating I atoms into the Si_{20} cages of the pi-Si NSs is possible (Appendix C). The electronic structure of the $I@Si_{100}H_{60}$ ND is shown in Fig. 1(c). By comparing the wave functions, we have confirmed that the electronic states labeled by li_I and hi_I originate in the l*i* and h*i* states of the $Si_{100}H_{60}$ ND, respectively, and that the I*p* state originated in the iodine 5*p* state. Due to the greater electronegativity of iodine, one valence electron is transferred from the host $Si_{100}H_{60}$ ND to the I atom so that the fourfold-degenerated $h1_I$ state of the $I@Si_{100}H_{60}$ ND is partially empty. In our calculations, the 4*d*, 5*s*, and 5*p* orbitals of an I atom are used as basis functions. The *s*, *p*, and *d* states belong to the A_g, T_{1u}, and H_g representations in the point group I_h, respectively. Therefore, the states of the $Si_{100}H_{60}$ ND, which belongs to the A_g (l1 state), T_{1u} (l2 state), and H_g (h3 state) representations, couple with the iodine *s*, *p*, and *d* states, respectively. However, the hybridization effect is relatively small.

The electronic structure of the $I_2@Si_{175}H_{90}$ ND is shown in Fig. 2(c). The electronic states labeled by Li_I and Hi_I originate in the L*i* and H*i* states of the $Si_{175}H_{90}$ ND, respectively. The I*pz* state originates in the iodine $5p_z$ state. Since two valence electrons are transferred from the $Si_{175}H_{90}$ ND to the two I atoms, the twofold-degenerated $H1_I$ state of the $I_2@Si_{175}H_{90}$ ND is partially empty. Although the wave functions of the iodine $5p_\perp$ ($5p_x$ and $5p_y$) state do not couple with the wave functions $\Psi_1^{H_u[E_1],\alpha}$ of the i-Si ND, they couple with the wave functions $\Psi_2^{H3,\alpha}$ of the pi-Si ND which is composed of the wave functions $\phi_2^{H_u[E_1],\alpha}$ (Appendix A). The symmetry reduction in the local icosahedral structure is a key to understand the hybridization effect. The structure of the pi-Si ND is strained due to the stress caused by linking i-Si NDs together. Actually, the symmetry of the Si_{20} cages is lowered from I_h (i-Si ND) to C_{5v} (pi-Si ND) (Appendix B). Therefore, although the wave functions $\phi_2^{H_u[E_1],\alpha}$ resemble the $\Psi_1^{H_u[E_1],\alpha}$, they are not the basis functions of the $H_u(I_h)$ representation but those of the $E_1(C_{5v})$ representation. Since the $5p_\perp$ state belongs to the E_1 representation in the point group C_{5v}, the wave functions $\phi_2^{H_u[E_1],\alpha}$ hybridize with the wave functions of the iodine $5p_\perp$ state. Due to the antibonding hybridization, the $H3_I$ state is upshifted and lies above the $H2_I$ state in energy. The hybridization effect on the other states near the Fermi level is relatively small.

The electronic structure of the $I_2@Si_{150}H_{60}$ NW is shown in Fig. 3(c). The $C1_I$, $V2_I$, and $V1_I$ bands of the $I_2@Si_{150}H_{60}$ NW originate in the C1, V2, and V1 bands of the $Si_{150}H_{60}$ NW, respectively. Since the valence electrons transfer from the host $Si_{150}H_{60}$ NW to the I atoms, the $V2_I$ and $V1_I$ bands are partially empty. Therefore, the $I_2@Si_{150}H_{60}$ NW is a metal. As in the case of the $I_2@Si_{175}H_{90}$ ND, due to the strain induced symmetry reduction of the $\phi_\infty^{H_u[E_{1u}],\alpha}$, the V2 band hybridizes with the iodine $5p_\perp$ state so that the bandwidth of the $V2_I$ band is enlarged, and the $V2_I^+(\Gamma)$ state lies above the $V1_I^+(\Gamma)$ state in energy.

Figure 8 compares the electronic band structures of partially I-doped pi-Si NWs, the $I_x@Si_{300}H_{120}$ NWs. As in the case of the $Na_x@Si_{300}H_{120}$ NWs, the electronic structures are calculated without geometry optimization because we have confirmed that there is no significant difference in the electronic structure near the Fermi level between the optimized $I_2@Si_{150}H_{60}$ NW and the initial structure, the optimized $Si_{150}H_{60}$ NW with an I atom placed at the gravity center of each Si_{20} cage. The band structure of the |OOOO| NW is obtained by folding the bands of the $I_2@Si_{150}H_{60}$ NW. Thus, the number of bands becomes double. We refer the upper parts of the $V1_I^+$ and $V2_I^+$ bands to the $V1_I^{++}$ and $V2_I^{++}$ bands, respectively. The $V1_I^{++}$ bands of partially I-doped pi-Si NWs are shifted downward in energy as the doping ratio decreases, because the hybridization effect between the $V2^{++}$ band and the iodine $5p_\perp$ state decreases. As a result, the $V2_I^{++}$ band of the |OXXX| NW lies below the $V1_I^{++}$ band. All the NWs are metal, but the bands which cross the Fermi energy depend on the doping pattern: |OOOO| ($V1_I^{++}$ and $V2_I^{++}$), |OOOX| ($V2_I^{++}$), |OOXX| ($V2_I^{++}$), |OXOX| ($V1_I^{++}$ and $V2_I^{++}$), and |OXXX| ($V1_I^{++}$). The optical dipole transition between the $C1_I^{--}(\Gamma)$ and $V2_I^{++}(\Gamma)$ states is prohibited in the $I_4@Si_{300}H_{120}$ NW because the contribution to the momentum matrix element $\langle\Psi^{C1_I^{--}(\Gamma)}|\hat{p}|\Psi^{V2_I^{++}(\Gamma)}\rangle$ from the *i*th i-Si ND completely cancels with the $(i+1)$th i-Si ND. However, the cancellation becomes incomplete in the partially I-doped pi-Si NWs. Thus, the optical dipole transition becomes possible in the partially I-doped pi-Si NWs, but the radiative recombination rates are relatively low ($<0.1\times10^6$ s^{-1}). The

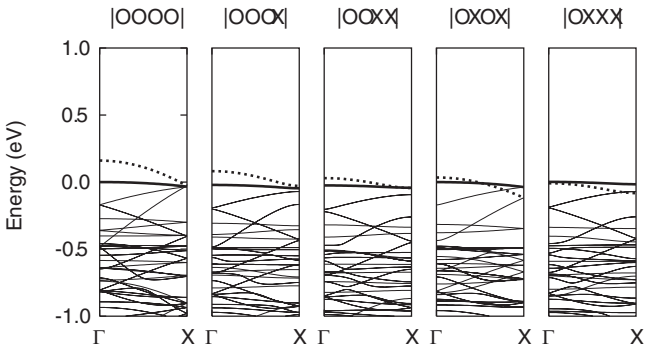

FIG. 8. The electronic band structures of partially I-doped pi-Si NWs, $I_x@Si_{300}H_{120}$ NWs. Energy is measured from the Fermi energy E_F, −4.98, −4.94, −4.91, −4.95, and −4.92 eV for |OOOO|, |OOOX|, |OOXX|, |OXOX|, and |OXXX| NWs, respectively. The $V1^{++}_{Na}$ and $V2^{++}_{Na}$ bands are drawn in bold solid and dotted lines, respectively.

transition energies of the |OOOX|, |OOXX|, |OXOX|, and |OXXX| NWs are 1.33, 1.20, 1.31, and 1.20 eV, respectively.

C. Electronic structure of NaI-doped systems

The electronic structure of the $NaI@Si_{175}H_{90}$ ND is shown in Fig. 2(d). The electronic states labeled by Li_{NaI} and Hi_{NaI} originate in the L*i* and H*i* states of the $Si_{175}H_{90}$ ND, respectively. Note that a Na atom is encapsulated into one Si_{20} cage and an I atom is encapsulated into the other cage. Due to the electropositivity of sodium and the electronegativity of iodine, one valence electron is transferred from the Na atom to the I atom. The HOMO and LUMO states of the NaI-doped pi-Si ND originate in the HOMO and LUMO states of the pi-Si ND, respectively. The band gap energy of the NaI-doped pi-Si ND (1.09 eV) is smaller than that of the guest-free pi-Si ND (1.60 eV). The other states are also affected by the NaI encapsulation. The $L3_{NaI}$ state is upshifted in energy far away from the range we depicted the energy levels. The $H3_{NaI}$ and $L3_{NaI}$ states are also downshifted out of the range. On the other hand, the $H6_{NaI}$ and $H8_{NaI}$ states are upshifted into the range.

The electronic band structure of the $NaI@Si_{150}H_{60}$ NW is shown in Fig. 3(d). The $C1_{NaI}$, $V1_{NaI}$, and $V2_{NaI}$ bands originate in the C1, V1, and V2 bands of the pi-Si NW, respectively. The valence electrons transfer from the Na atoms to the I atoms, and the NaI-doped pi-Si NW is a direct-gap semiconductor. The band gap energy of the NaI-doped pi-Si NW (1.09 eV) is smaller than that of the guest-free pi-Si NW (2.09 eV). The V2 band hybridizes with the iodine $5p_\perp$ state so that the $V2_{NaI}$ is upshifted in energy. However, the hybridization effect is small compared with the $I_2@Si_{150}H_{60}$ NW, and the energy of the $V2^+_{NaI}(\Gamma)$ state is almost the same as the $V1^+_{NaI}(\Gamma)$ state. As in the case of partially I-doped pi-Si NWs, the incomplete cancellation in the momentum matrix element occurs. Thus, the optical dipole transition between the $C1^-_{NaI}(\Gamma)$ and $V2^+_{NaI}(\Gamma)$ states is possible with a radiative recombination rate of 0.5×10^6 s^{-1}.

V. SUMMARY

We have reported a systematic first-principles study of the electronic and optical properties of guest-free, Na-doped, I-doped, and NaI-doped pi-Si NSs. The band gap energy of the guest-free pi-Si NS increases from 1.20, 1.60, to 2.09 eV as the number of linked i-Si NDs N_l decreases from ∞ (polyicosahedral $Si_{150}H_{60}$ NW), 2 (polyicosahedral $Si_{175}H_{90}$ ND), to 1 (icosahedral $Si_{100}H_{60}$ ND) due to the quantum confinement effect. Although the pi-Si NW is a direct-band-gap semiconductor, the optical dipole transition between the LUMO and HOMO states is prohibited in the pi-Si NSs. The analyses of electronic wave functions show that the wave functions of the pi-Si ND and the pi-Si NW can be expressed as linear combination of wave functions which resemble to the wave functions of the i-Si ND. The comparison of the electronic band structure of the pi-Si NW with the similar-size pentagonal $Si_{30}H_{10}$ NW and crystalline diamond $Si_{45}H_{20}$ NW reveals that the band gap energy and the effective masses of the Si NW strongly depend on the arrangement of Si atoms. We have compared the stability of the nanowires as a function of the hydrogen chemical potential and found that the hydrogen chemical potential could be a key for synthesizing the pi-Si NW and the pent-Si NW.

The calculated encapsulation energy suggests that the encapsulation of Na or I atoms into the Si_{20} cages of pi-Si NSs is possible. In Na-doped pi-Si NSs, the valence electron transfers from the Na atom to the Si framework due to the greater electropositivity of sodium. As a result, the LUMO-HOMO optical dipole transition becomes possible in the $Na@Si_{100}H_{60}$ ND and $Na_2@Si_{175}H_{90}$ ND with transition energies of 0.56 and 0.37 eV, respectively. The $Na_2@Si_{150}H_{60}$ NW is a metal (half-filled $C1_{Na}$ band), while the corresponding guest-free $Si_{150}H_{60}$ NW is a semiconductor. The Na-doped pi-Si NW is stable against the Peierls distortion. The nature of the electronic band structure of partially Na-doped piSi NWs strongly depends on the doping ratio and doping pattern. The |OXXX|, |OXOX|, and |OOOX| NWs are metals as in the case of the |OOOO| NW. On the other hand, the |OOXX| NW is a direct-band-gap semiconductor. The LUMO-HOMO optical dipole transition is possible in the |OOXX| NW with a transition energy of 0.24 eV.

In I-doped pi-Si NSs, the valence electron transfers from the Si framework to the I atom due to the greater electronegativity of iodine, which results in the metallic $I_2@Si_{150}H_{60}$ NW (partially empty $V1_I$ and $V2_I$ bands). The strain in the local icosahedral structures caused by linking icosahedra together enables the hybridization of the V2 band and the iodine $5p_\perp$ (p_x and p_y) state. As a result, the bandwidth of the $V2_I$ band is enlarged, and the $V2^+_I(\Gamma)$ state lies above the $V1^+_I(\Gamma)$ state in energy. The optical dipole transition between the $C1^{--}_I$ and $V2^{++}_I$ states is possible in partially I-doped pi-Si NWs due to the incomplete cancellation of the momentum matrix element, but the radiative recombinations are relatively low ($<0.1\times10^{-6}$ s^{-1}).

In NaI-doped pi-Si NSs, the valence electron transfers from the Na atom to the I atom due to the electropositivity of sodium and the electronegativity of iodine. The band gap energies of the $NaI@Si_{175}H_{90}$ ND (1.09 eV) and $NaI@Si_{150}H_{60}$ NW (1.09 eV) are decreased compared with the corresponding guest-free pi-Si ND (1.60 eV) and pi-Si NW (2.06 eV), respectively. The V2 band hybridizes with the iodine $5p_\perp$ state so that the $V2_{NaI}$ is upshifted in energy.

However, the hybridization effect is small compared with the $I_2@Si_{150}H_{60}$ NW, and the energy of the $V2^+_{NaI}(\Gamma)$ state is almost the same as the $V1^+_{NaI}(\Gamma)$ state. The optical dipole transition between the $C1^-_{NaI}(\Gamma)$ and $V2^+_{NaI}(\Gamma)$ states is possible with a transition energy of 1.09 eV.

Our results demonstrate that the electronic and optical properties of the pi-Si NSs can be tuned by doping appropriate guest atoms and controlling the size. The tunability is suitable for the building blocks of the future nanoscale Si-based optoelectronic devices. The pi-Si NS has not been identified experimentally yet, but the synthesis of the pi-Si NS would open up new avenues for science and technology. We hope that our results will stimulate further studies for synthesizing the pi-Si NS.

ACKNOWLEDGMENTS

The authors wish to thank T. Ikeshoji and T. Nakamura for fruitful discussions, and R. DeVane for a critical reading of the paper. This work is supported in part by METI (as part of the Nanoelectronics project) and the Next Generation Super Computing Project, the Nanoscience Program. The computations are, in part, carried out at the Research Center for Computational Science, National Institute of Natural Sciences.

APPENDIX A: ELECTRONIC WAVE FUNCTIONS

By comparing electron wave functions of the i-Si ND (1-PINS) to those of the pi-Si ND (2-PINS) and pi-Si NW (∞-PINS), we find that the wave function $\Psi^{\mu}_{N_l}$ of the N_l-PINS is well expressed as linear combinations of wave functions $\phi^{\nu}_{N_l}$ which resemble to the wave function Ψ^{ν}_1 of the i-Si ND, where μ and ν are the indices of electronic state. Our findings described below will help us understand the effects of encapsulating Na and I atoms into the Si_{20} cages.

First, we discuss the wave functions of the i-Si ND. The l1, l2, h1, h2, and h3 states of the i-Si ND belong to the A_g, T_{1u}, G_g, H_u, and H_g representations of the point group I_h, respectively. The wave functions of the degenerated states can be classified into several groups. For example, when the symmetry is lowered from I_h to $C_{5v}(D_{5d})$, the G_g representation splits as

$$G_g \downarrow C_{5v}(D_{5d}) = E_1(E_{1g}) + E_2(E_{2g}). \tag{A1}$$

According to this relation, the wave functions of the fourfold-degenerated h1 state are classified into two groups:

$$\{\Psi_1^{G_g[E_1]}\} = \{\Psi_1^{G_g[E_1],1}, \Psi_1^{G_g[E_1],2}\} \tag{A2}$$

and

$$\{\Psi_1^{G_g[E_2]}\} = \{\Psi_1^{G_g[E_2],1}, \Psi_1^{G_g[E_2],2}\}. \tag{A3}$$

The classification for the other states is summarized in Table III. The wave functions classified above are useful in analyzing the wave functions of the N_l-PINS.

The isosurface and contour maps of the electron wave functions of LUMO of the i-Si ND (l1 state), pi-Si ND (L1 state), and pi-SiNW [$C1^-(\Gamma)$ state] are depicted in Fig. 9 using XCrysden.[60] We find from Fig. 9 that the LUMO wave function Ψ_2^{L1} of the pi-Si ND is a bonding orbital of wave functions $\phi_2^{A_g}$, which resemble the LUMO wave function $\Psi_1^{A_g}$ of the i-Si ND, and is expressed as

TABLE III. The classification of wave functions of the icosahedral $Si_{100}H_{60}$ ND.

State	Group
l2	$\{\Psi_1^{T_{1u}[A_1]}\}$, $\{\Psi_1^{T_{1u}[E_1]}\}$
l1	$\{\Psi_1^{A_g}\}$
h1	$\{\Psi_1^{G_g[E_1]}\}$, $\{\Psi_1^{G_g[E_2]}\}$
h2	$\{\Psi_1^{H_u[A_2]}\}$, $\{\Psi_1^{H_u[E_1]}\}$, $\{\Psi_1^{H_u[E_2]}\}$

$$\Psi_2^{L1}(\mathbf{r}) = \phi_2^{A_g}(\mathbf{r} - \mathbf{r}_u) + \phi_2^{A_g}(\hat{\sigma}_h(\mathbf{r} - \mathbf{r}_l)), \tag{A4}$$

where $\hat{\sigma}_h$ is the operator of the reflection about a plane which is perpendicular to the fivefold symmetry axis (z axis) and passes through the origin. The $\mathbf{r}_u$ and $\mathbf{r}_l$ are the positions of the gravity centers of the upper and lower Si_{20} cages, respectively. Similarly, the LUMO wave function Ψ_{∞}^{L1} of the pi-Si NW is a bonding orbital of wave functions $\phi_{\infty}^{A_g}$ and is expressed as

$$\Psi_{\infty}^{L1}(\mathbf{r}) = \sum_i^{\infty} \phi_{\infty}^{A_g}(\hat{\sigma}_h^i(\mathbf{r} - \mathbf{r}_i)), \tag{A5}$$

where $\mathbf{r}_i$ is the position of the gravity center of the ith Si_{20} cage.

The wave functions of HOMO of the pi-Si ND (H1 state) and pi-Si NW [$V1^+(\Gamma)$ state] are expressed with linear combinations of wave functions which resemble the HOMO wave functions of the i-Si ND (h1 state) as well. However, the situation is rather complicated because the h1 state belongs to the fourfold-degenerated G_g representation while the H1 and $V1^+(\Gamma)$ states are twofold degenerated. As is summarized in Table III, the wave functions of the G_g state are classified into $\{\Psi_1^{G_g[E_1]}\}$ and $\{\Psi_1^{G_g[E_2]}\}$. We find from Fig. 10 that the HOMO wave functions $\Psi_2^{H1,\alpha}$ of the pi-Si ND are antibonding orbitals of wave functions $\phi_2^{G_g[E_2],\alpha}$ and are expressed as

$$\Psi_2^{H1,\alpha}(\mathbf{r}) = \phi_2^{G_g[E_2],\alpha}(\mathbf{r} - \mathbf{r}_u) - \phi_2^{G_g[E_2],\alpha}(\hat{\sigma}_h(\mathbf{r} - \mathbf{r}_l)). \tag{A6}$$

Note that the wave functions $\phi_2^{G_g[E_1],\alpha}$ have nothing to do with the H1 state of the pi-Si ND. Similarly, the HOMO wave functions $\Psi_{\infty}^{V1^+(\Gamma),\alpha}$ of the pi-Si NW are antibonding orbitals of wave functions $\phi_{\infty}^{G_g[E_2],\alpha}$ and are expressed as

$$\Psi_{\infty}^{V1^+(\Gamma),\alpha}(\mathbf{r}) = \sum_i^{\infty} (-1)^i \phi_{\infty}^{G_g[E_2],\alpha}(\hat{\sigma}_h^i(\mathbf{r} - \mathbf{r}_i)). \tag{A7}$$

Note that we implicitly assume in Eq. (1) that the LUMO and HOMO wave functions of the N_l-PINS are expressed as linear combinations of wave functions which resemble the LUMO and HOMO wave functions of the i-Si ND, respectively.

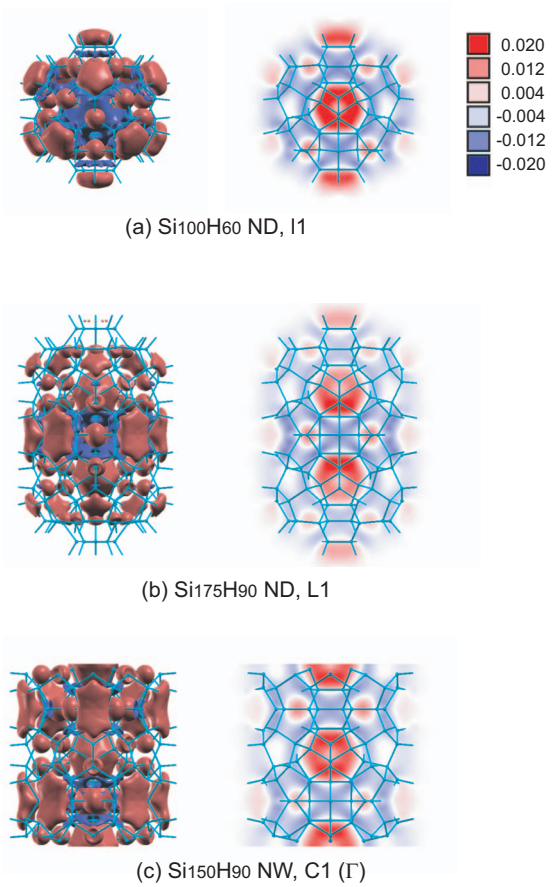

FIG. 9. (Color) The isosurface (± 0.01 electrons/$a_0^{3/2}$) and contour maps of the LUMO wave functions: (a) the l1 state of the icosahedral $Si_{100}H_{60}$ ND, (b) the L1 state of the polyicosahedral $Si_{175}H_{90}$ ND, and (c) the C1$^-$(Γ) state of the polyicosahedral $Si_{150}H_{60}$ NW, where a_0 is the Bohr radius. The color plane divides the structure into two parts and contains the fivefold symmetry axis.

The wave functions $\phi_2^{A_g}$ and $\phi_2^{T_{1u}[A_1]}$ are mixed in the wave function of the L2 state of the pi-Si ND. Actually, we have confirmed that the wave function Ψ_2^{L2} is well expressed as

$$\Psi_2^{\mathrm{L2}}(\mathbf{r}) = \phi_2^{A_g+T_{1u}[A_1]}(\mathbf{r}-\mathbf{r}_u) - \phi_2^{A_g+T_{1u}[A_1]}(\hat{\sigma}_h(\mathbf{r}-\mathbf{r}_l)), \tag{A8}$$

where

$$\phi_2^{A_g+T_{1u}[A_1]}(\mathbf{r}) = \frac{1}{\sqrt{2}}\phi_2^{A_g}(\mathbf{r}) + \frac{1}{\sqrt{2}}\phi_2^{T_{1u}[A_1]}(\mathbf{r}). \tag{A9}$$

Similarly, the wave function of the C1(X) state of the pi-Si NW is well expressed as

$$\Psi_\infty^{\mathrm{C1(X)}}(\mathbf{r}) = \sum_i^\infty (-1)^{\mathrm{floor}(i/2)}\phi_\infty^{A_g+T_{1u}[A_1]}(\hat{\sigma}_h^i(\mathbf{r}-\mathbf{r}_i)). \tag{A10}$$

Note that the floor (x) is the largest integer less than or equal to x.

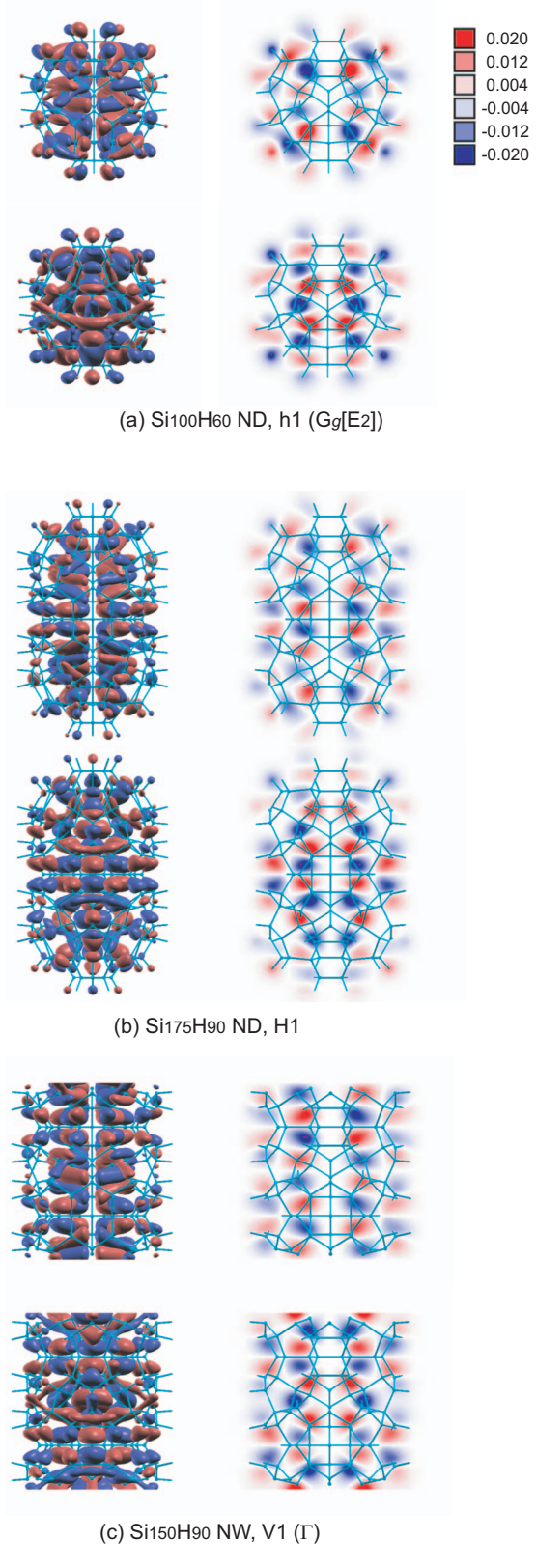

FIG. 10. (Color) The isosurface (± 0.01 electrons/$a_0^{3/2}$) and contour maps of the HOMO wave functions: (a) the h1 ($G_g[E_2]$) state of the icosahedral $Si_{100}H_{60}$ ND, (b) the H1 state of the polyicosahedral $Si_{175}H_{90}$ ND, and (c) the V1$^+$(Γ) state of the polyicosahedral $Si_{150}H_{60}$ NW, where a_0 is the Bohr radius. The color plane divides the structure into two parts and contains the fivefold symmetry axis.

TABLE IV. The wave functions of the polyicosahedral $Si_{175}H_{90}$ ND.

$\Psi_2^{L4,\alpha}(\mathbf{r})$	=	$\phi_2^{T_{1u}[E_1],\alpha}(\mathbf{r}-\mathbf{r}_u)$	+	$\phi_2^{T_{1u}[E_1],\alpha}(\hat{\sigma}_h(\mathbf{r}-\mathbf{r}_l))$
$\Psi_2^{L3}(\mathbf{r})$	=	$\phi_2^{T_{1u}[A_1]}(\mathbf{r}-\mathbf{r}_u)$	+	$\phi_2^{T_{1u}[A_1]}(\hat{\sigma}_h(\mathbf{r}-\mathbf{r}_l))$
$\Psi_2^{L2}(\mathbf{r})$	=	$\phi_2^{A_g+T_{1u}[A_1]}(\mathbf{r}-\mathbf{r}_u)$	−	$\phi_2^{A_g+T_{1u}[A_1]}(\hat{\sigma}_h(\mathbf{r}-\mathbf{r}_l))$
$\Psi_2^{L1}(\mathbf{r})$	=	$\phi_2^{A_g}(\mathbf{r}-\mathbf{r}_u)$	+	$\phi_2^{A_g}(\hat{\sigma}_h(\mathbf{r}-\mathbf{r}_l))$
$\Psi_2^{H1,\alpha}(\mathbf{r})$	=	$\phi_2^{G_g[E_2],\alpha}(\mathbf{r}-\mathbf{r}_u)$	−	$\phi_2^{G_g[E_2],\alpha}(\hat{\sigma}_h(\mathbf{r}-\mathbf{r}_l))$
$\Psi_2^{H2,\alpha}(\mathbf{r})$	=	$\phi_2^{H_u[E_2],\alpha}(\mathbf{r}-\mathbf{r}_u)$	+	$\phi_2^{H_u[E_2],\alpha}(\hat{\sigma}_h(\mathbf{r}-\mathbf{r}_l))$
$\Psi_2^{H3,\alpha}(\mathbf{r})$	=	$\phi_2^{H_u[E_1],\alpha}(\mathbf{r}-\mathbf{r}_u)$	−	$\phi_2^{H_u[E_1],\alpha}(\hat{\sigma}_h(\mathbf{r}-\mathbf{r}_l))$
$\Psi_2^{H4,\alpha}(\mathbf{r})$	=	$\phi_2^{G_u[E_1],\alpha}(\mathbf{r}-\mathbf{r}_u)$	+	$\phi_2^{G_u[E_1],\alpha}(\hat{\sigma}_h(\mathbf{r}-\mathbf{r}_l))$

Our results including the other states are summarized in Tables IV and V.

APPENDIX B: Si_{20} CAGE STRUCTURE

The Si_{20} cage of the i-Si ND is an equilateral dodecahedron with I_h symmetry. The Si_{20} cages of the pi-Si ND and the pi-Si NW would be strained due to the stress caused by linking i-Si NDs together. As we have shown in Sec. IV B, the strain in the Si_{20} cage, or the symmetry breakdown, is a key to understand how I atoms affect the electronic structure of pi-Si NSs. In order to characterize the Si_{20} cage structure, we consider two half spheroids joined at the equator,

$$f(\mathbf{r},a,c_+,c_-) \equiv \begin{cases} \dfrac{x^2+y^2}{a^2}+\dfrac{z^2}{c_+^2} & \text{if } z>0 \\ \dfrac{x^2+y^2}{a^2}+\dfrac{z^2}{c_-^2} & \text{if } z<0 \end{cases} = 1, \quad \text{(B1)}$$

near whose surface the Si atoms are located. We search for a set of parameters (a,c_+,c_-) which minimize the error,

$$E_r = \frac{1}{20}\sum_{i=1}^{20}[f(\mathbf{r}_i,a,c_+,c_-)-1]^2, \quad \text{(B2)}$$

where $\mathbf{r}_i$ is the position of the ith Si atom measured from the gravity center of the Si_{20} cage. Note that, for an equilateral dodecahedral Si_{20} cage, $a=c_+=c_-$ and $E_r=0$.

TABLE V. The wave functions of the polyicosahedral $Si_{150}H_{60}$ NW. Note that the floor (x) is the largest integer less than or equal to x.

$\Psi_\infty^{C1^+(\Gamma)}(\mathbf{r})$	=	$\Sigma_i^\infty \phi_\infty^{T_{1u}[A_1]}(\hat{\sigma}_h^i(\mathbf{r}-\mathbf{r}_i))$
$\Psi_\infty^{C1(X)}(\mathbf{r})$	=	$\Sigma_i^\infty (-1)^{\text{floor}(i/2)} \phi_\infty^{A_g+T_{1u}[A_1]}(\hat{\sigma}_h^i(\mathbf{r}-\mathbf{r}_i))$
$\Psi_\infty^{C1^-(\Gamma)}(\mathbf{r})$	=	$\Sigma_i^\infty \phi_\infty^{A_g}(\hat{\sigma}_h^i(\mathbf{r}-\mathbf{r}_i))$
$\Psi_\infty^{V1^+(\Gamma),\alpha}(\mathbf{r})$	=	$\Sigma_i^\infty (-1)^i \phi_\infty^{G_g[E_2],\alpha}(\hat{\sigma}_h^i(\mathbf{r}-\mathbf{r}_i))$
$\Psi_\infty^{V1(X),\alpha}(\mathbf{r})$	=	$\Sigma_i^\infty (-1)^{\text{floor}(i/2)} \phi_\infty^{G_g[E_2]+H_u[E_2],\alpha}(\hat{\sigma}_h^i(\mathbf{r}-\mathbf{r}_i))$
$\Psi_\infty^{V1^-(\Gamma),\alpha}(\mathbf{r})$	=	$\Sigma_i^\infty \phi_\infty^{G_g[E_2],\alpha}(\hat{\sigma}_h^i(\mathbf{r}-\mathbf{r}_i))$
$\Psi_\infty^{V2^+(\Gamma),\alpha}(\mathbf{r})$	=	$\Sigma_i^\infty (-1)^i \phi_\infty^{H_u[E_1],\alpha}(\hat{\sigma}_h^i(\mathbf{r}-\mathbf{r}_i))$
$\Psi_\infty^{V2(X),\alpha}(\mathbf{r})$	=	$\Sigma_i^\infty (-1)^{\text{floor}(i/2)} \phi_\infty^{H_u[E_1]+G_g[E_1],\alpha}(\hat{\sigma}_h^i(\mathbf{r}-\mathbf{r}_i))$
$\Psi_\infty^{V2^-(\Gamma),\alpha}(\mathbf{r})$	=	$\Sigma_i^\infty \phi_\infty^{H_u[E_1],\alpha}(\hat{\sigma}_h^i(\mathbf{r}-\mathbf{r}_i))$

TABLE VI. The Si_{20} cage structure. The errors E_r defined by Eq. (B2) are below 0.0001. The parameters for the upper cage are shown for pi-Si NDs: the neighbor cage exists in the negative direction.

	a (Å)	c_+ (Å)	c_- (Å)
$Si_{100}H_{60}$ ND	3.256	3.256	3.256
$Na@Si_{100}H_{60}$ ND	3.261	3.261	3.261
$I@Si_{100}H_{60}$ ND	3.274	3.273	3.273
$Si_{175}H_{90}$ ND	3.279	3.196	3.165
$Na_2@Si_{175}H_{90}$ ND	3.285	3.207	3.169
$I_2@Si_{175}H_{90}$ ND	3.298	3.225	3.184
$Si_{150}H_{60}$ NW	3.323	3.058	3.058
$Na_2@Si_{150}H_{60}$ NW	3.323	3.087	3.086
$I_2@Si_{150}H_{60}$ NW	3.336	3.110	3.110

Our results summarized in Table VI reveal that the Si_{20} cage of the i-Si ND corresponds to a sphere of 3.256 Å in radius. The Si_{20} cage of the pi-Si NW is shrunken in the direction of the wire axis by about 6% ($|3.058/3.256-1|$) and bulged out perpendicular to the axis by about 2% ($|3.323/3.256-1|$). Thus, the Si_{20} cage of the pi-Si NW corresponds to a spheroid with D_{5d} symmetry. The symmetry $c_+=c_-$ is broken in the Si_{20} cage of the pi-Si ND, and the joined spheroid is more prolate toward the adjacent i-Si ND. Note that the symmetry of the Si_{20} cage is C_{5v}.

We also analyze the Si_{20} cage structure of Na- or I-doped pi-Si NSs. In all the cases, the Si_{20} cages are slightly expanded compared with guest-free cages as is summarized in Table VI.

APPENDIX C: ENCAPSULATION ENERGY

Sodium and iodine atoms can be encapsulated into the Si_{20} and Si_{24} cages of the bulk type-I Si clathrate (Si_{46}).[28,30] On the other hand, it is unclear whether these atoms can be encapsulated into the Si_{20} cages of pi-Si NSs or not. For discussing the feasibility of encapsulation, we calculated the energy per atom of encapsulating Na and I atoms into the cages of host H defined as

$$E_{\text{enc}} = \frac{E(\text{Na}_x\text{I}_y@\text{H}) - xE(\text{Na}) - yE(\text{I}) - E(\text{H})}{(x+y)}, \quad \text{(C1)}$$

where $E(\text{X})$ is the total energy of X molecule and x and y are the numbers of Na and I atoms in the unit cell, respectively. The encapsulation energies are summarized in Table VII. In calculating the total energies of isolated Na and I atoms, the spin-polarization effects are taken into account within the local spin-density approximation,[42,43] and the counterpoise correction is applied to minimize the basis set superposition error. As a reference, we also calculated the encapsulation energies for bulk $Na_8@Si_{46}$ and $I_8@Si_{46}$. Our results show that the encapsulation energy of a Na atom decreases with increasing the number of linked icosahedra: $Na@Si_{100}H_{60}$

TABLE VII. The encapsulation energy E_{enc} (eV).

Bulk $Na_8@Si_{46}$	0.84	bulk $I_8@Si_{46}$	−1.73		
$Na@Si_{100}H_{60}$ ND	0.91	$I@Si_{100}H_{60}$ ND	−0.89		
$Na_2@Si_{175}H_{90}$ ND	0.71	$I_2@Si_{175}H_{90}$ ND	−1.09	$NaI@Si_{175}H_{90}$	−0.70
$Na_2@Si_{150}H_{60}$ NW	0.52	$I_2@Si_{150}H_{60}$ NW	−1.17	$NaI@Si_{150}H_{60}$	−0.68

ND (0.91 eV), $Na_2@Si_{175}H_{90}$ ND (0.71 eV), and $Na_2@Si_{150}H_{60}$ NW (0.52 eV). This means that the encapsulation of Na atoms is energetically more feasible for longer pi-Si NSs. Although the positive values indicate that the encapsulation of Na atoms is energetically less favorable, we expect that the encapsulation is possible because the values are comparable to the bulk $Na_8@Si_{46}$ (0.84 eV), which has been synthesized experimentally. Note that the positive values are consistent with the E_{enc} of the $Na@Si_{20}H_{20}$ cluster.[61] All the encapsulation energies for I-doped and NaI-doped pi-Si NSs are negative values, indicating that the encapsulation is energetically favorable. Note that $E_{enc}(NaI@H) < \{E_{enc}(Na_2@H) + (E_{enc}(I_2@H))\}/2$ is explained by the ionic bond between Na and I atoms.

*k-nishio@aist.go.jp

[1] N.-M. Park, C.-J. Choi, T.-Y. Seong, and S.-J. Park, Phys. Rev. Lett. **86**, 1355 (2001).
[2] K. Nishio, J. Kōga, T. Yamaguchi, and F. Yonezawa, Phys. Rev. B **67**, 195304 (2003).
[3] K.-M. Ho, A. A. Shvartsburg, B. Pan, Z.-Y. Lu, C.-Z. Wang, J. G. Wacker, J. L. Fye, and M. F. Jarrold, Nature (London) **392**, 582 (1998).
[4] T. Bachels and R. Schäfer, Chem. Phys. Lett. **324**, 365 (2000).
[5] Y. Zhao and B. I. Yakobson, Phys. Rev. Lett. **91**, 035501 (2003).
[6] Y. Zhao, Y.-H. Kim, M.-H. Du, and S. B. Zhang, Phys. Rev. Lett. **93**, 015502 (2004).
[7] K. Nishio, T. Morishita, W. Shinoda, and M. Mikami, J. Chem. Phys. **125**, 074712 (2006).
[8] K. Nishio, T. Morishita, W. Shinoda, and M. Mikami, Phys. Rev. B **72**, 245321 (2005).
[9] S. Iijima, Jpn. J. Appl. Phys., Part 1 **26**, 357 (1987).
[10] S. Iijima, Jpn. J. Appl. Phys., Part 1 **26**, 365 (1987).
[11] F. S. Khan and J. Q. Broughton, Phys. Rev. B **43**, 11754 (1991).
[12] J. Pan and M. V. Ramakrishna, Phys. Rev. B **50**, 15431 (1994).
[13] J. Wang, X. Zhou, G. Wang, and J. Zhao, Phys. Rev. B **71**, 113412 (2005).
[14] E. Kaxiras, Phys. Rev. Lett. **64**, 551 (1990).
[15] B.-X. Li, J.-H. Liu, and S.-C. Zhan, Eur. Phys. J. D **32**, 59 (2005).
[16] H. Hiura, T. Miyazaki, and T. Kanayama, Phys. Rev. Lett. **86**, 1733 (2001).
[17] T. Miyazaki, H. Hiura, and T. Kanayama, Phys. Rev. B **66**, 121403(R) (2002).
[18] V. Kumar, Comput. Mater. Sci. **30**, 260 (2004).
[19] A. K. Singh, V. Kumar, and Y. Kawazoe, Phys. Rev. B **71**, 115429 (2005).
[20] Q. Sun, Q. Wang, P. Jena, B. K. Rao, and Y. Kawazoe, Phys. Rev. Lett. **90**, 135503 (2003).
[21] N. Gonzalez Szwacki and B. I. Yakobson, Phys. Rev. B **75**, 035406 (2007).
[22] J. Tersoff, Phys. Rev. B **39**, R5566 (1989).
[23] M. Menon and E. Richter, Phys. Rev. Lett. **83**, 792 (1999).
[24] B.-X. Li, P. L. Cao, R. Q. Zhang, and S. T. Lee, Phys. Rev. B **65**, 125305 (2002).
[25] J. Bai, X. C. Zeng, H. Tanaka, and J. Y. Zeng, Proc. Natl. Acad. Sci. U.S.A. **101**, 2664 (2004).
[26] S. Yamada and H. Fujiki, Jpn. J. Appl. Phys., Part 2 **45**, L837 (2006).
[27] P. V. Avramov, A. A. Kuzubov, A. S. Fedorov, P. B. Sorokin, F. N. Tomilin, and Y. Maeda, Phys. Rev. B **75**, 205427 (2007).
[28] J. S. Kasper, P. Hagenmuller, M. Pouchard, and C. Cros, Science **150**, 1713 (1965).
[29] H. Fukuoka, K. Ueno, and S. Yamanaka, J. Organomet. Chem. **611**, 543 (2000).
[30] E. Reny, S. Yamanaka, C. Cros, and M. Pouchard, Chem. Commun. (Cambridge) **2000**, 2505.
[31] S. Yamanaka, E. Enishi, H. Fukuoka, and M. Yasukawa, Inorg. Chem. **39**, 56 (2000).
[32] G. B. Adams, M. O'Keeffe, A. A. Demkov, O. F. Sankey, and Y.-M. Huang, Phys. Rev. B **49**, 8048 (1994).
[33] S. Saito and A. Oshiyama, Phys. Rev. B **51**, 2628 (1995).
[34] K. Moriguchi, M. Yonemura, A. Shintani, and S. Yamanaka, Phys. Rev. B **61**, 9859 (2000).
[35] D. Connétable, V. Timoshevskii, E. Artacho, and X. Blase, Phys. Rev. Lett. **87**, 206405 (2001).
[36] B. Marsen and K. Sattler, Phys. Rev. B **60**, 11593 (1999).
[37] R. Kagimura, R. W. Nunes, and H. Chacham, Phys. Rev. Lett. **95**, 115502 (2005).
[38] U. Landman, R. N. Barnett, A. G. Scherbakov, and P. Avouris, Phys. Rev. Lett. **85**, 1958 (2000).
[39] S. Sirichantaropass, V. M. García-Suárez, and C. J. Lambert, Phys. Rev. B **75**, 075328 (2007).
[40] P. Hohenberg and W. Kohn, Phys. Rev. **136**, B864 (1964).
[41] W. Kohn and L. J. Sham, Phys. Rev. **140**, A1133 (1965).
[42] D. M. Ceperley and B. J. Alder, Phys. Rev. Lett. **45**, 566 (1980).
[43] J. P. Perdew and A. Zunger, Phys. Rev. B **23**, 5048 (1981).
[44] P. E. Blöchl, Phys. Rev. B **41**, 5414 (1990).
[45] N. Troullier and J. L. Martins, Phys. Rev. B **43**, 1993 (1991).
[46] T. Ozaki, Phys. Rev. B **67**, 155108 (2003).
[47] T. Ozaki and H. Kino, Phys. Rev. B **69**, 195113 (2004).
[48] J. M. Soler, E. Artacho, J. D. Gale, A. García, J. Junquera, P. Ordejón, and D. Sánchez-Portal, J. Phys.: Condens. Matter **14**, 2745 (2002).
[49] The code, OpenMX, pseudo-atomic basis functions, pseudopotentials are available from http://www.openmx-square.org/

[50] P. Csaszar and P. Pulay, J. Mol. Struct. **31**, 114 (1984).
[51] Each i-Si ND is rotated 180° about the wire axis against its adjacent i-Si NDs.
[52] Note that LDA underestimates the energy of unoccupied states. Actually, in our theoretical framework, the band gap energy of the bulk cd-Si is 0.51 eV, which is smaller than experimental value of 1.17 eV by 0.66 eV.
[53] A. J. Read, R. J. Needs, K. J. Nash, L. T. Canham, P. D. J. Calcott, and A. Qteish, Phys. Rev. Lett. **69**, 1232 (1992).
[54] D. L. Dexter, in *Solid State Physics*, edited by F. Seitz and D. Turnbull (Academic, New York, 1958), Vol. 6, p. 358.
[55] T. Akiyama, K. Nakamura, and T. Ito, Phys. Rev. B **74**, 033307 (2006).
[56] J. E. Northrup, Phys. Rev. B **44**, 1419 (1991).
[57] R. E. Peierls, *Quantum Theory of Solids* (Oxford University Press, New York, 1955).
[58] J. W. Mintmire, B. I. Dunlap, and C. T. White, Phys. Rev. Lett. **68**, 631 (1992).
[59] D. Connétable, G.-M. Rignanese, J.-C. Charlier, and X. Blase, Phys. Rev. Lett. **94**, 015503 (2005).
[60] A. Kokalj, Comput. Mater. Sci. **28**, 155 (2003); code available from http://www.xcrysden.org/
[61] C.-Y. Zhang, H.-S. Wu, and H. Jiao, Chem. Phys. Lett. **410**, 457 (2005).